Electron heating and phase space signatures at strong and weak quasi-perpendicular shocks

A. J. Hull, J. D. Scudder, L. A. Frank, and W. R. Paterson

Department of Physics and Astronomy, University of Iowa, Iowa City

M. G. Kivelson

Institute of Geophysics and Planetary Physics, University of California, Los Angeles
Department of Earth and Space Sciences, University of California, Los Angeles

Abstract. The coherent effects implied by the magnetic field jump $[B]$ and the deHoffmann-Teller frame (HTF) potential jump $[\Phi^{HT}]$ on electron heating and phase space signatures at shocks of different strengths are presented. Of particular interest is whether these coherent effects have sufficiently different signatures to explain the observed preferential transverse heating in weak shocks while still producing nearly isotropic heating for strong shocks. Vlasov-Liouville mappings of an upstream electron core-halo distribution function f_1, modified to reflect electron mirroring, are employed to determine the downstream electron distribution function f_2. Electrons within the shock are treated as a laminar Vlasov guiding center ordered fluid. These mappings demonstrate that the coherent effects play a major role in producing, at all pitch angles, characteristic electron distribution function signatures observed behind strong and weak shocks and thus significantly impact electron heating. A favorable test of the Vlasov-Liouville mapping concept was performed using detailed upstream and downstream distribution functions at a weak bow shock observed by Galileo on the second Earth flyby. Especially noteworthy is that the Vlasov-Liouville procedure recovers the anisotropic inflationary signatures of the observed downstream electron distribution function.

1. Introduction

Although electron heating across collisionless shocks has attracted much attention for many years, the problem of predicting the electron temperature changes across collisionless fast mode shocks remains an open question. Particle codes supported by high time resolution in situ plasma measurements have proven to be valuable tools in elucidating ion heating and shock structure on ion scales but have difficulty in recovering observed electron heating signatures. In particular, hybrid simulations with kinetic ions and massless fluid electrons played a major role in determining the ion dissipation mechanism while recovering the salient features of the shock field structure [*Leroy et al.*, 1982; *Leroy and Winske*, 1983; *Goodrich*, 1985] as caused by broken ion Larmor orbits. Yet, by design, hybrid codes cannot determine the dominant electron heating mechanism. Recent simulations by *Savoini and Lembege* [1994], with expensive explicit full particle codes, have reproduced the electron flat-top distribution function for the first

time. *Savoini and Lembege* [1994] claim that the DC fields are responsible for the flat-top signatures and electron heating, whereas wave particle effects play a relatively unimportant role. However, their results are incomplete because their simulations use a very low ion to electron mass ratio which artificially enhances coupling between electrons and ions. Consequently, the increased electron-ion coupling affects the dispersive properties of the waves [*Krauss-Varban et al.*, 1995] and leads to unphysical particle heating. A two-dimensional (2-D) implicit full particle simulation [*Krauss-Varban et al.*, 1995], using a more realistic mass ratio, recovered the adiabatic behavior of electrons across a strong shock. Nevertheless, this simulation did not recover the ubiquitously observed electron flat-top distribution.

Observations of weak interplanetary shocks (e.g., downstream-upstream magnetic field ratio $B_2/B_1 \to 1$) have shown that transverse electron heating exceeds that parallel to the magnetic field [*Feldman et al.*, 1983a]. The more isotropically inflated flat-top electron distribution functions are observed behind strong shocks (e.g., $B_2/B_1 \to 4$) as in the Earth's bow shock [*Montgomery et al.*, 1970; *Feldman et al.*, 1983b; *Scudder et al.*, 1986a]. These observations have led to the proposal of several mechanisms to explain the electron

signatures observed in strong and weak shocks. Early attention focused on microinstabilities and subsequent turbulence as a mechanism for converting directed energy into random energy via waves [e.g., *Biskamp*, 1973; *Davidson and Krall*, 1977; *Wu et al.*, 1984; *Winske et al.*, 1985, 1987]. Proponents of the microinstability paradigm sought to replace collisions with wave particle interactions as the dominant momentum transfer and heating mechanism in collisionless shocks. One principal class of waves thought to occur at collisionless shocks and impact electron heating was the ion acoustic type of modes [e.g., *Biskamp*, 1973; *Galeev*, 1976; *Papadopoulos*, 1977; *Greenstadt and Fredricks*, 1979]. These are high-frequency ($\omega \sim \omega_{\mathrm{pi}}$) electrostatic modes which derive their free energy from sufficiently large cross-field drifts. However, observations [*Scudder et al.*, 1986a] have demonstrated that the electron-ion drift is not sufficiently large to meet the threshold required to excite ion acoustic turbulence. Low-frequency ($\omega \lesssim \Omega_{\mathrm{ci}}$) modes can occur, but there is insufficient time for these types of waves to grow to significant amplitudes within the shock layer and play a major role in particle heating [*Scudder et al.*, 1986c; *Winske et al.*, 1987]. Instabilities in the lower-hybrid regime ($\omega \sim \Omega_{\mathrm{LH}}$) which include the modified two-stream instability, the kinetic cross-field streaming instability and the lower-hybrid drift instability may be important [*Winske et al.*, 1985; *Scudder et al.*, 1986c; *Winske et al.*, 1987], though how important these are in heating electrons at collisionless shocks still requires clarification.

It is generally agreed that the required entropy change across collisionless shocks is the result of microturbulence. Yet, before one can determine electron heating due to microinstabilities, it is necessary to determine the impact of the macroscopic electric and magnetic fields. In addition, theoretical studies suggest that the coherent effects on electron heating implied by the macroscopic electric and magnetic fields present in collisionless shocks may be significant [*Goodrich and Scudder*, 1984]. One recent suggestion invoked diverging electron trajectories as a mechanism for the coherent energization of electrons [*Balikhin et al.*, 1993; *Balikhin and Gedalin*, 1994]. In this picture, sufficiently inhomogeneous crossed electric and magnetic fields are supposed to break guiding center ordered behavior of electrons and cause the electron trajectories to diverge. It is argued that the guiding center approximation of magnetic moment conservation no longer applies. Hence the energization of the demagnetized electrons is suggested to be responsible for the electron temperature change across the shock. However, the 2-D implicit full particle simulation by *Krauss-Varban et al.* [1995] found no evidence of additional heating due to diverging electron trajectories as suggested by *Balikhin et al.* [1993] and *Balikhin and Gedalin* [1994]. Moreover, this heating mechanism requires shocks to possess length scales $\lesssim c/\omega_{\mathrm{pe}}$ which are much smaller than those typically documented by multiple spacecraft observations.

In actuality the electric and magnetic fields are observed [*Russell et al.*, 1982; *Scudder et al.*, 1986b] to vary on scales of the order of the convecting ion inertial length (e.g., U_n/Ω_{ci}) which are much larger than the electron gyroradius. Even the main shock ramp's logarithmic scale length is typically ~ 10 c/ω_{pe}, contrary to the nonadiabatic premise. As a consequence, electron behavior is constrained by the first adiabatic invariant, and the electrons remain magnetized throughout the layer. Moreover, electron bulk flow in the HTF is to a good approximation field-aligned [*Scudder*, 1987]. This simplification allows a quantitative calculation of the behavior of magnetized electrons in the macroscopic fields within the shock layer essential to electron heating. In particular, the detailed study by *Scudder et al.* [1986c] demonstrated the importance of the HTF potential in heating electrons by employing a Vlasov-Liouville mapping technique for a parallel cut of the electron distribution function across a supercritical quasi-perpendicular fast mode shock and by exploiting the conservation of magnetic moment of electrons throughout the layer. Wave particle effects, although required, were found to play a minor role in electron heating by irreversibly relaxing the electron distribution function to a more stable state. Other aspects of the Liouville mapping technique have been employed to estimate the HTF potential jump across fast [*Schwartz et al.*, 1988] and slow mode shocks [*Schwartz et al.*, 1987] using just a piece of the electron distribution function. Because these studies utilize only a piece or $\mu = 0$ cut of the electron distribution function, they are incomplete. The impact of the DC fields on electron heating signatures at all energies and pitch angles of the electron distribution function is the focus of the present work.

This paper extends the work of *Scudder et al.* [1986c], *Scudder* [1995], and *Schwartz et al.* [1988] and clarifies the observations of *Feldman et al.* [1983a, b]. It illustrates how characteristic signatures observed in electron velocity distribution functions at all pitch angles and thus electron heating in the strong and weak limit of collisionless fast mode shocks can be explained by the interaction of magnetized electrons with the macroscopic fields. First, Vlasov-Liouville mappings of model distribution functions across shocks of different strengths are employed to show how the coherent energization processes manifest themselves in the asymptotic electron velocity distribution functions f_1 and f_2 at strong and weak shocks. As a further test of the method, a detailed upstream electron velocity distribution function measured by the Galileo plasma instrument [*Frank et al.*, 1992] at a weak quasi-perpendicular Earth bow shock (discussed by *Kivelson et al.* [1995]) is theoretically mapped to the downstream side and compared to observation. The difference between the present study and previous studies employing similar techniques is that the present work applies the Vlasov-Liouville mapping technique to the full electron velocity distribution function (rather than just a cut) thereby demonstrating the effectiveness of the macroscopic fields in producing the entire velocity distribution function signatures observed behind the weak shock even before any wave particle scattering is considered.

2. Theoretical Mapping of Mirror Modified Core-Halo Distribution Functions

The theoretical mapping procedure used in this paper solves the steady state Vlasov equation by the method of characteristics in the guiding center approximation. Thus the shock layer in our study is treated as time stationary. We work in the HTF because the electron bulk flow is approximately field-aligned as stated above and because it is the most natural frame for describing electron kinematics. In this frame of reference, electrons gain the full electrostatic potential energy jump across the shock because electron drifts perpendicular to the shock normal do no work since the tangential electrostatic field vanishes in this frame [*Goodrich and Scudder*, 1984].

In this section we assess the impact of coherent effects on electron heating and phase space signatures by using a model upstream distribution function, f_1. f_1 is mapped to the downstream side of the shock using Liouville's theorem to obtain the downstream distribution function, f_2 which is then compared to f_1. In addition to conservation of energy, the mapping procedure uses the following simplifying assumptions. First, the electrons are assumed to remain magnetized everywhere throughout the shock layer. In addition, the field-aligned flow approximation is invoked. With these assumptions the magnetic moment is conserved, and the electron bulk flow remains along the same magnetic flux tube of force as the electrons traverse the shock. The last assumption is that the differentials of the HTF potential $\delta \Phi^{HT}$ are proportional to the magnetic intensity differentials δB, an approximation motivated by theory [*Alfvén and Fälthammer*, 1963; *Whipple*, 1977] and data [*Scudder et al.*, 1986c]. This assumption implies an equation of state of the form

$$[\Phi^{HT}] = \kappa[B] \tag{1}$$

where κ is a strict constant. Brackets are used to denote the change of a physical quantity across the shock layer (e.g., $[X] \equiv X_2 - X_1$ where X_1 and X_2 are the upstream and downstream asymptotic values of the physical quantity X).

The equation of state can be motivated by arguments based on the zero normal current condition required for time stationary shock layers. Zero normal current requires the normal number flux between electrons and ions to be equal. However, electrons, being magnetized, can be mirrored by the increasing magnetic field, whereas ions, because of their large gyroradius, tend to stream across the layer. The different inertial responses of electrons and ions to the shock field structure result in an electric field which acts as a feedback mechanism that counters electron mirroring and accelerates the bulk of the electrons to maintain a steady state of equal electron and ion normal number fluxes. Thus an increase in the HTF potential coincides with an increase in the magnetic field intensity. A large fraction

of the electron population must get through in order for the electron and ion normal number fluxes to be equal; therefore we believe that κ should scale as $O\left(\frac{kT_{e\perp}}{eB}\big|_{sw}\right)$.

The characteristic curves along which f is a constant are defined by the electron orbits. However, not all of the electron orbits can access the downstream side of the shock. In order to determine the phase space accessible and inaccessible to electrons as they traverse the layer we examine the constraints of conservation of energy and magnetic moment:

$$E = \frac{1}{2}m_e\left(v_\perp{}^2(x) + v_\parallel{}^2(x)\right) - e\Phi^{HT}(x) = \text{const} \tag{2}$$

$$\mu = \frac{\frac{1}{2}m_e v_\perp{}^2(x)}{B(x)} = \text{const} \tag{3}$$

where $v_\perp(x)$ and $v_\parallel(x)$ are the local components of the HTF velocity of the electrons perpendicular and parallel to the magnetic field, respectively. Electrons that have access to the downstream side of the shock must have $v_\parallel{}^2(x) \geq 0$ for all x connecting the upstream and downstream asymptotic states. Assuming a monotonic magnetic field profile and $\delta\Phi^{HT} \propto \delta B$, this reduces to the condition that the downstream parallel velocity must be nonnegative (e.g., $v_{2\parallel} \geq 0$). With this simplification it is easy to show that accessibility to the downstream side of the shock requires electron orbits to have upstream velocities within the hyperboloid of one sheet defined by

$$v_{1\perp}{}^2 \leq \frac{B_1}{[B]}\left(v_{1\parallel}{}^2 + v_\Phi{}^2\right) \tag{4}$$

with

$$v_\Phi{}^2 = \frac{2e}{m_e}[\Phi^{HT}]. \tag{5}$$

Here $v_{1\perp}$ and $v_{1\parallel}$ are the perpendicular and parallel components of the upstream electron velocity in the HTF, respectively. Under strict equality, (4) defines a modified loss cone separatrix in velocity space that partitions the upstream phase space into four distinct regions. The modified loss cone separatrix, familiar from auroral physics [*Knight*, 1973; *Whipple*, 1977] and studies of electron distributions at the Earth's foreshock [*Fitzenreiter et al.*, 1990], can be thought of as the generalization of the standard loss cone separatrix caused by the parallel electric field. A generic modified loss cone separatrix anticipated in the upstream region is indicated by the dashed lines in Figure 1. Region I represents solar wind particles that have access to the downstream side of the shock; region II represents incoming solar wind particles that eventually get mirrored by the shock layer; region III represents particles mirrored by the shock; and region IV represents particles originally from the downstream side of the shock that leak into the upstream side.

Using the information gained from energy and magnetic moment conservation laws, we construct the upstream electron velocity distribution function with appropriate mirroring signatures [*Fitzenreiter et al.*, 1990]. An appropriate mirror-modified upstream distribution
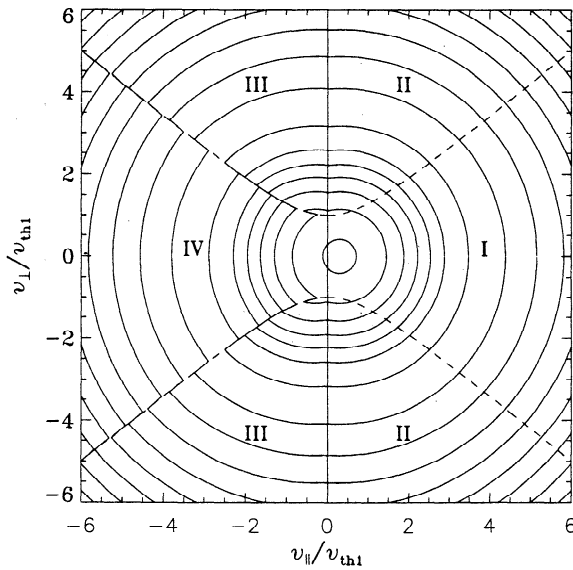
Figure 1. Model upstream electron distribution function with modified loss cone separatrix indicated by dashed lines. The upstream distribution function with appropriate mirroring signatures must reflect the boundary conditions of the system that connect to each of the four distinct regions. Region I represents solar wind particles that have access to the downstream side of the shock, regions II and III represent the mirrored population and region IV represents particles from the downstream side of the shock that leak into the upstream side of the shock. In Figure 1 $v_\parallel$ and $v_\perp$ are normalized by the upstream thermal speed v_{th1}

reiter et al., 1990]. Values for the shape parameters η, $\omega_\parallel$, $\omega_\perp$, ψ_c, and ψ_h are chosen so that the density, thermal speed, and bulk speed as moments of $f_1(\mathbf{v_1})$ constructed from f_{ch} represent typical upstream solar wind conditions.

3. Results of the Theoretical Mapping of Model Distribution Functions

Examples of model electron distribution functions in $(v_\parallel, v_\perp)$ space for a strong shock case with $\theta_{Bn1} = 75.8°$, $B_2/B_1 = 3.26$, and $M_f = 3.8$ are illustrated in Fig-
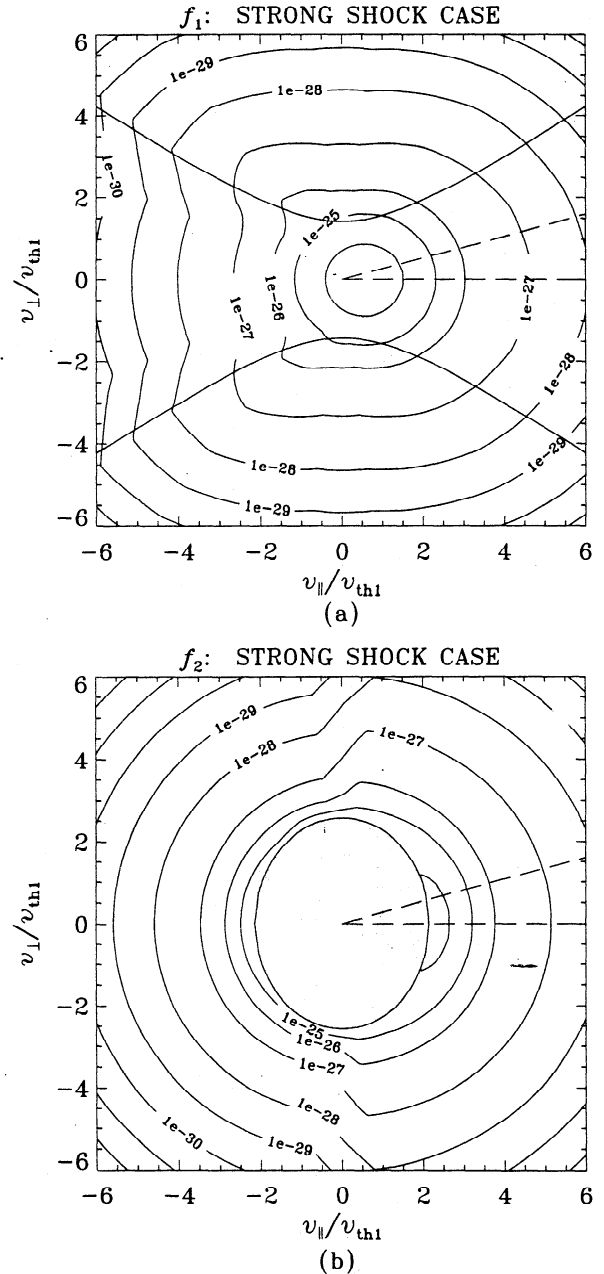
Figure 2. (a) Upstream and (b) downstream model electron velocity distribution functions in $v_\parallel - v_\perp$ space at a strong shock with $\theta_{Bn1} = 75.8°$, $B_2/B_1 = 3.26$, and $M_f = 3.8$. These distribution functions are smoothed over an angular resolution $\Delta\phi = 15.0°$.

function must reflect the boundary conditions of the system that connect to each of the four distinct regions (see Figure 1). Thus we can set $f_1(v_{1\parallel}, v_{1\perp}) = f_{\mathrm{ch}}(v_{1\parallel}, v_{1\perp})$ in regions I and II in order to represent the incoming particles from the solar wind. The empirically motivated solar wind distribution used to construct $f_1(\mathbf{v_1})$ is given by [Feldman et al., 1975]

$$f_{\mathrm{ch}}(\mathbf{v_1}) = \frac{\eta(1-\delta)}{(\sqrt{\pi})^3 \omega_\parallel \omega_\perp^2} \exp\left(-\frac{(v_{1\parallel}-\psi_c)^2}{\omega_\parallel^2} - \frac{v_{1\perp}^2}{\omega_\perp^2}\right)$$

$$+ \frac{\eta\delta}{(\gamma\sqrt{\pi})^3 \omega_\parallel \omega_\perp^2} \exp\left(-\frac{(v_{1\parallel}-\psi_h)^2}{\gamma^2\omega_\parallel^2} - \frac{v_{1\perp}^2}{\gamma^2\omega_\perp^2}\right) \quad (6)$$

where δ controls the halo density fraction and $\gamma^2 = T_h/T_c$ controls the halo-core temperature ratio. The shape parameters η, $\omega_\parallel$, $\omega_\perp$, ψ_c, and ψ_h determine the total density, core parallel thermal speed, core perpendicular thermal speed and HTF parallel bulk speeds of the core and halo populations of f_{ch}, respectively. Particles reflected by the shock determine the form of the distribution in region III. In this region we may set $f_1(v_{1\parallel}, v_{1\perp}) = f_{\mathrm{ch}}(-v_{1\parallel}, v_{1\perp})$, enforcing the mirror with region II. In region IV we set $f_1(v_{1\parallel}, v_{1\perp}) = f_{\mathrm{ch}}(v_{1\parallel}, v_{1\perp})$. This restates the assumption that contributions to this region in phase space from electrons that traverse the curved shock on the downstream side can leak back to the upstream side on field lines [Fitzen-

ures 2a and 2b for upstream and downstream locations, respectively. Here θ_{Bn1} is the angle between the upstream magnetic field and the shock normal, and M_f is the fast mode Mach number. The exact Vlasov modeled upstream and downstream distribution functions have discontinuities that are not present in observed distribution functions. Observed electron distribution functions are irretrievably smoothed by the detector's finite energy and angular resolution. In order to make the model predictions more realistic the upstream and downstream distribution functions of Figures 2a and 2b have been smoothed over the angular resolution of an ISEE class detector $\sqrt{\Delta\Omega} \sim 15°$. The smoothing angle is indicated by the dashed wedge in Figures 2a and 2b. Present in the downstream distribution function is an elliptic but nearly isotropic void (shaded) given by

$$\frac{v_{2\parallel}^2}{v_\Phi^2} + \frac{v_{2\perp}^2}{\frac{v_\Phi^2}{\beta^2}} \leq 1 \qquad (7)$$

that represents a region of downstream phase space that has no characteristics that connect to the upstream side [*Scudder*, 1995]. Here $v_{2\parallel}$ and $v_{2\perp}$ are the parallel and perpendicular components of the downstream electron HTF velocity and $\beta^2 = \frac{[B]}{B_2}$. The inflationary signatures of the downstream electron distribution function in the region outside of the elliptical void can be inferred from the shape of the void. The shape of the void depends on the parameter β which is a measure of the shock strength. In the case of strong shocks, β approaches the limit of $\sqrt{3}/2$, resulting in a nearly circular void in $(v_\parallel, v_\perp)$ space. This is apparent in the strong shock example where $\beta = 0.7$. The nearly isotropic inflation of phase space by the DC forces is consistent with the similar signatures typically found in electron distribution functions observed at strong shocks. In contrast, β approaches zero for weak shocks which results in a flatter ellipse. Example model upstream and downstream electron distribution functions in $(v_\parallel, v_\perp)$ space for a weak shock case with $\theta_{Bn1} = 61.2°$, $B_2/B_1 = 1.25$, and $M_f = 1.2$ are illustrated in Figures 3a and 3b, respectively. In this case the elliptical void is flatter ($\beta = 0.2$) than its stronger shock counterpart which implies a more anisotropic downstream electron distribution function. In other words, the macroscopic forces in this example tend to inflate the downstream phase space preferentially in the transverse degree of freedom.

To further illustrate the inflationary signatures associated with the model electron distribution functions, Figures 4 and 5 depict upstream-downstream comparisons between parallel ($v_\perp = 0$) and perpendicular ($v_\parallel = 0$) cuts in the plasma rest frame for the modeled strong and weak shock cases, respectively. The crosses reflect the downstream distribution, and the solid curves reflect the upstream distribution. The theoretical void region is bounded by the vertical dashed lines in both Figures 4 and 5. Figures 4 and 5 illustrate different patterns of heating to be expected in the strong and weak shock limit by coherent forces. In particular, the coherent fields act in such a way as to inflate

particle phase space more isotropically in the strong shock limit while preferring perpendicular inflation in the weak shock limit even without invoking wave particle effects as anticipated by *Scudder* [1995]. These heating signatures obtained via the Vlasov mapping model are consistent with the inflationary signatures found in observations.

The temperature of the downstream distribution function can be estimated by using a maximal trapping approximation [*Morse*, 1965; *Forslund and Shonk*, 1970; *Scudder et al.*, 1986c], which is an attempt to es-
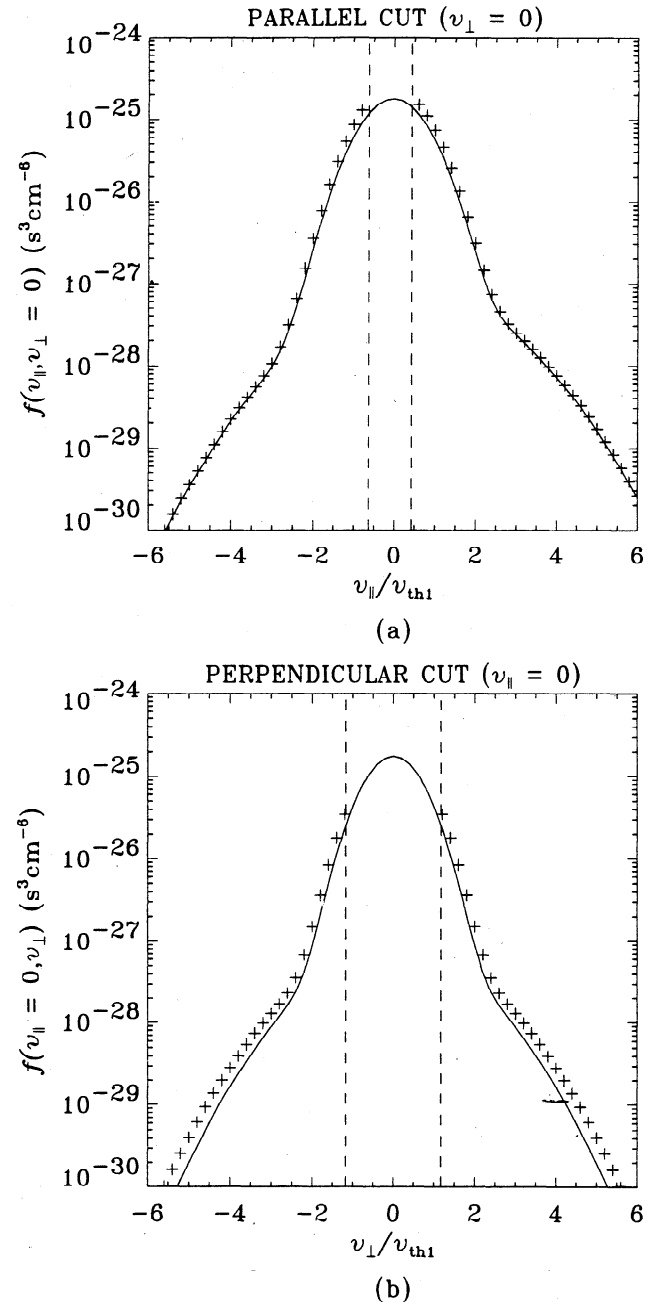

(a)

(b)
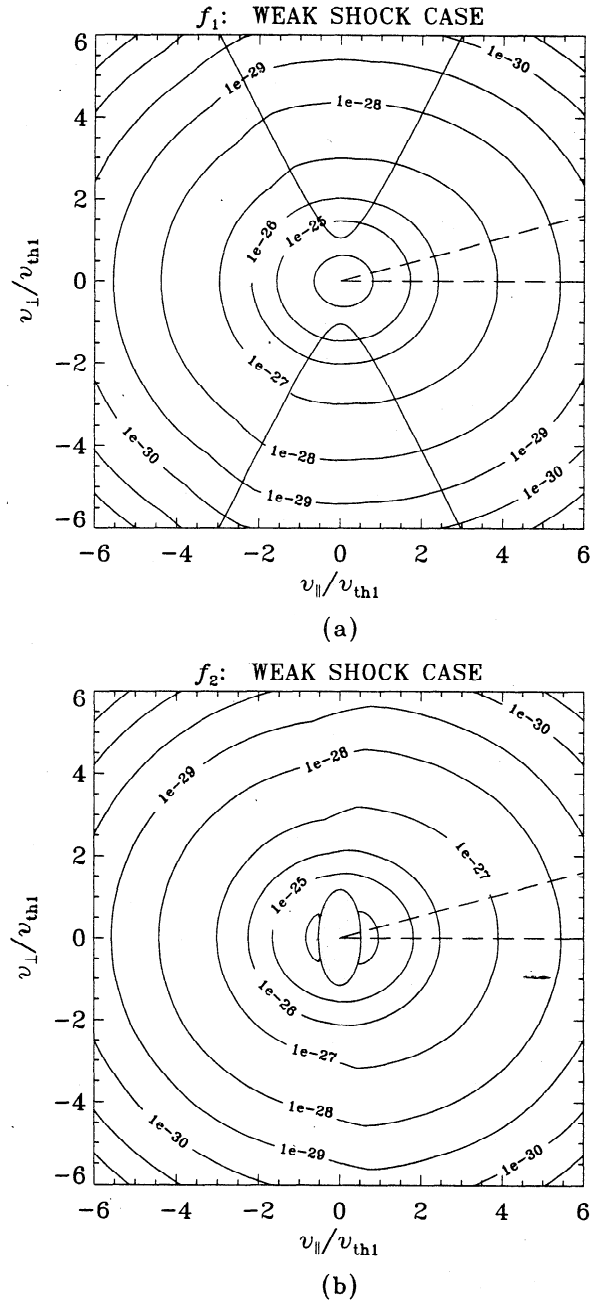
Figure 3. (a) Upstream and (b) downstream model electron velocity distribution functions at a weak shock with $\theta_{Bn1} = 61.2°$, $B_2/B_1 = 1.25$, and $M_f = 1.2$. These distribution functions are smoothed over an angular resolution $\Delta\phi = 15.0°$.

PARALLEL CUT ($v_\perp = 0$)

(a)

PERPENDICULAR CUT ($v_\parallel = 0$)

(b)
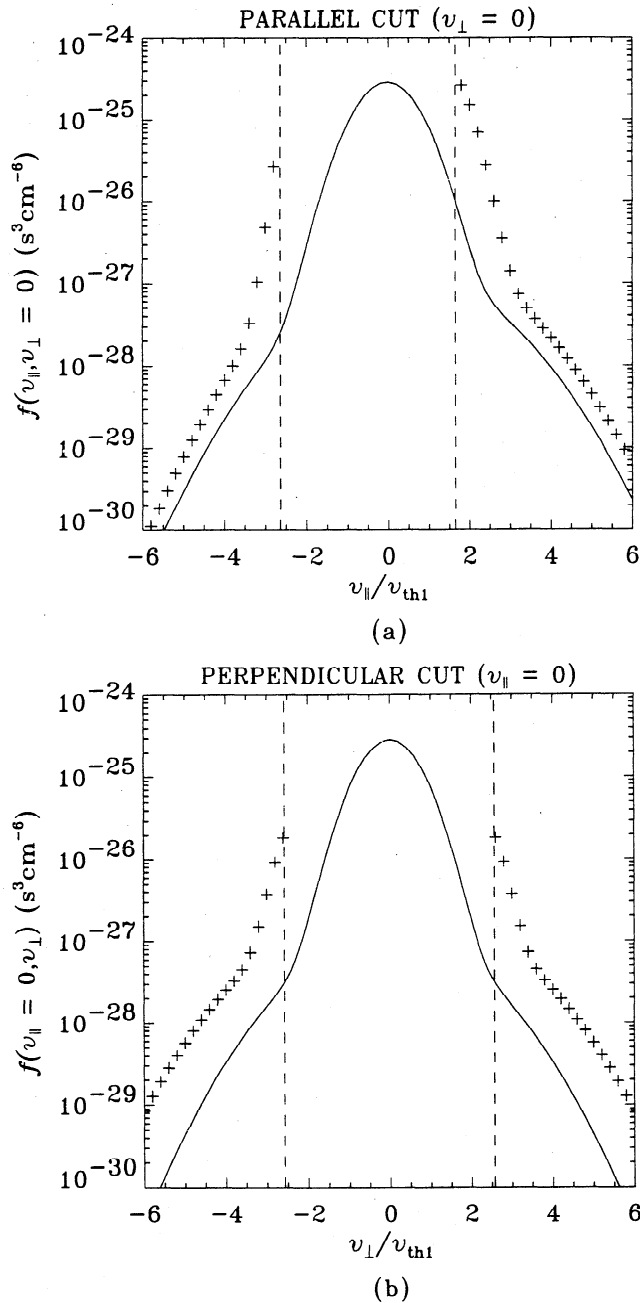
Figure 4. (a) Parallel cut of the electron downstream distribution function(crosses) as contrasted with the upstream parallel cut (solid curve) for the strong shock case. (b) Perpendicular cut of the electron downstream distribution function (crosses) as contrasted with upstream perpendicular cut (solid curve) for the strong shock case. The distribution function cuts are in the plasma rest frame. The vertical dashed lines in Figures 4a and 4b indicate the location of the theoretical void.

along the perimeter of the void using a flat trapping model in such a way as to get the Rankine-Hugoniot (RH) expectation of the downstream electron density. This approach reflects the pervasive flat-topped distribution functions found in observations and is consistent with macroscopic conservation laws. Temperature change calculations with this model using the maxi-

PARALLEL CUT ($v_\perp = 0$)

(a)

PERPENDICULAR CUT ($v_\parallel = 0$)

(b)

timate the filling of the void by trapped electrons (e.g., electrons from the magnetosheath that cannot access the upstream side of the shock but have access to the void region in the downstream velocity space). To estimate the downstream temperature, we fill the void to a level proportional to the average distribution function

Figure 5. (a) Parallel cut of the electron downstream distribution function(crosses) as contrasted with the upstream parallel cut (solid curve) for the weak shock case. (b) Perpendicular cut of the electron downstream distribution function(crosses) as contrasted with upstream perpendicular cut for (solid curve) the weak shock case. The distribution function cuts are in the plasma rest frame. The vertical dashed lines in Figures 5(a) and 5(b) bound the theoretical void region.

mal trapping approximation resulted in a 7% change in the parallel temperature and an 11% change in the perpendicular temperature for the weak shock example. On the other hand, the strong shock case resulted in temperature enhancements of roughly 165% and 160% in the parallel and perpendicular degree of freedom, respectively. These results are consistent with the trends found in observations of parallel and perpendicular temperature changes at strong and weak shocks as reported, for example, by *Feldman et al.* [1983a]. The quantitative results of the mapping procedure applied to model electron distribution functions cannot be directly compared to observations. A better test of the Vlasov procedure is to contrast the mapping of observed upstream electron distribution functions with observed downstream distribution functions. In section 4 we apply the Vlasov-Liouville mapping procedure to an upstream electron distribution function of a weak shock observed at a remote region of the Earth's bow shock. Of particular interest is that the Vlasov procedure recovers the anisotropic inflationary signatures of the observed downstream electron distribution function as suggested by the above study.

4. Observed Weak Shock Parameter Determination

As an additional test the Vlasov-Liouville mapping technique is demonstrated with detailed upstream and downstream distribution functions observed by the plasma science (PLS) instrument [*Frank et al.*, 1992] as

Galileo traversed a weak shock at $\sim$0800 UT on December 5, 1992, during the second Earth flyby. Data from the Galileo magnetometer instrument [*Kivelson et al.*, 1992] and PLS have been used along with the RH equations to constrain important shock parameters needed for the mapping (see Table 1). *Whang's* [1987] formulation of the jump relations are solved to yield the downstream jump conditions for fast mode shocks given the upstream plasma β, the Alfvén Mach number M_A, and the angle between the upstream magnetic field and the shock normal θ_{Bn1}. Determination of β requires knowledge of the temperature of the cold supersonic solar wind ions. Although the solar wind ions are detected with PLS, the velocity distributions are not sufficiently well resolved to determine ion temperatures accurately. Therefore an ion temperature of 6×10^4 K has been assumed using the statistical $T_i - U_i$ relation [*Burlaga and Ogilvie*, 1973] for an ion bulk flow of 350 km s^{-1}. From the electron and ion temperature, density and magnetic field data, the upstream plasma β is estimated to be 0.64. The Alfvén speed V_A is inferred to be 74 $\pm$ 3 km s^{-1}. While V_A only includes the proton contribution, variation of the He^{++} density from 0% to 10% of the proton density did not significantly affect the results of this study. Given β, the RH jump equations determine the density ratio n_2/n_1 and the magnetic field ratio B_2/B_1 as a function of the fast mode Mach number M_f and θ_{Bn1}. Empirical estimates of n_2/n_1 and B_2/B_1 allow inferences of M_f and θ_{Bn1}. Figure 6 displays RH consistent contours of n_2/n_1 (solid curves) and B_2/B_1 (dashed curves) as a function of M_f

Table 1. Asymptotic Shock Parameters

Parameter	Upstream	Downstream	Units
Magnetic field intensity, B	8.75 $\pm$ .25[a]	11.0 $\pm$ .3[a]	nT
Magnetic field unit vector, GSE, $\hat{b}$	(-.9056, .3379, -.2565)	(-.8872, .3642, -.2832)	
Angle between $\hat{n}$ and $\hat{b}$, θ_{Bn}	54° $\pm$20°[b], 71°[e]	62° $\pm$15°[b], 75°[e]	
Electron density, n_e	6.7 $\pm$ .7[a]	8.5 $\pm$ .9[a]	cm^{-3}
Perpendicular electron temperature, $T_{e\perp}$	1.3 $\pm$ .1[a]	1.6 $\pm$ .1[a]	10^5 K
Parallel electron temperature, $T_{e\parallel}$	1.9 $\pm$ .1[a]	1.9 $\pm$ .1[a]	10^5 K
Electron temperature, T_e	1.5 $\pm$ .1	1.7 $\pm$ .1	10^5 K
Ion temperature, T_i	$\sim$ 6[c]	$\sim$ 8[d]	10^4 K
Electron beta, β_e	0.46	0.41	
Ion beta, β_i	$\sim$ 0.18	$\sim$ 0.19	
Plasma beta, β	0.64	0.6	
Fast mode Mach number, M_f	1.22 $\pm$ .04[b], 1.20[e]	0.84	
Alfvén Mach number, M_A	1.43 $\pm$ .07[b], 1.46[e]	1.02 $\pm$ .16	
Alfvén speed, V_A	74 $\pm$ 3	82 $\pm$ 3	km s^{-1}
Normal bulk speed, U_n	106 $\pm$ 7[b], 108[e]	84 $\pm$ 13	km s^{-1}
HTF potential jump, [Φ^{HT}]	—	3.4 $\pm$ $^{0.9}_{0.1}$[f], 3.0 $\pm$ 1.3[g]	V

[a]Observations.
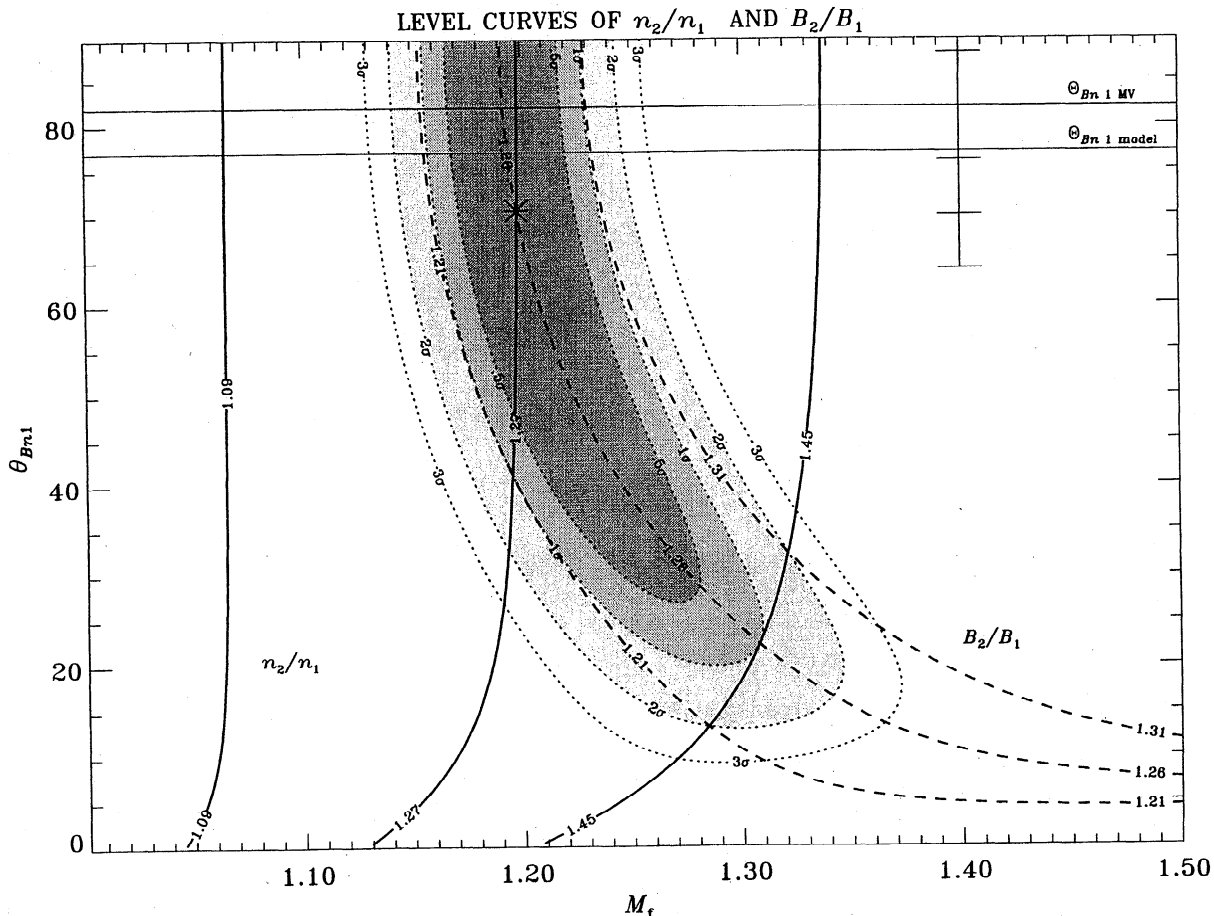[b]Estimated from plasma and field data using RH jump relations as leverage.
[c]Estimated using $T_i - V_i$ relation.
[d]Estimated using polytrope closure relation with $\gamma = 5/3$.
[e]Optimal value assumed in the χ^2 fit procedure of this paper.
[f]Result of the χ^2 fit procedure.
[g]Estimated from ambipolar electric field term of electron momentum equation.

LEVEL CURVES OF n_2/n_1 AND B_2/B_1

Figure 6. Level curves of n_2/n_1 (solid) and B_2/B_1 (dash-dotted) as a function of M_f and θ_{Bn1}. Only contours consistent with the empirical range of these ratios are indicated. The statistical weight $\mathcal{P}$ (indicated by the shaded regions out to 3 standard deviations) associated with the ordered pairs (M_f, θ_{Bn1}) shows the range of θ_{Bn1} and M_f consistent with the observed n_2/n_1 and B_2/B_1. The asterisk indicates the most probable M_f and θ_{Bn1} used to test the Vlasov mapping procedure. Independent determinations of θ_{Bn1} by a minimum variance technique and a bow shock model are indicated by the horizontal solid lines.

and θ_{Bn1}. Only contours consistent with the empirical range of these ratios are indicated. Assuming the errors in n_2/n_1 and B_2/B_1 obey Gaussian statistics, the statistical weight associated with the ordered pairs (M_f, θ_{Bn1}) is given by

$$\mathcal{P} = \frac{1}{2\pi\sigma_{B_r}\sigma_{n_r}} \exp\left[\frac{-\left(\frac{B_2}{B_1} - \overline{\frac{B_2}{B_1}}\right)^2}{2\sigma_{B_r}^2} - \frac{\left(\frac{n_2}{n_1} - \overline{\frac{n_2}{n_1}}\right)^2}{2\sigma_{n_r}^2}\right] \quad (8)$$

In (8), σ_{B_r} and σ_{n_r} represent the empirical errors in the magnetic field ratio and the density ratio estimated to be 0.05 and 0.18, respectively. Level curves out to 3 standard deviations are indicated in Figure 6. Using $\mathcal{P}$, the fast mode Mach number M_f and θ_{Bn1} are estimated to be $1.22 \pm .04$ and $54° \pm 20°$, respectively. The Alfvén Mach number is inferred to be $1.43 \pm .07$. Given V_A and constraints on M_A, the upstream relative speed along the shock normal $U_{n1} = (\mathbf{U_e} - \mathbf{V_{shock}}) \cdot \mathbf{n}$ is found to be 106 ± 7 km s^{-1}. Even though M_A, M_f and U_{n1} are tightly constrained, θ_{Bn1} is still only loosely

determined by this method. The θ_{Bn1} was estimated to be $82° \pm 6°$ via a minimum variance technique (indicated by upper horizontal solid line with error bars out to 3 standard deviations in Figure 6) using high time resolution magnetometer data only over the interval connecting the upstream and downstream data sets used in the mapping procedure. However, such a technique by itself can be unreliable [*Lepping and Argentiero*, 1971; *Abraham-Shrauner*, 1972]. A conic section model of the Earth's bow shock extended to these remote regions predicts a shock normal $\hat{n} = [.37, .76, .54]$ in GSE (L. Bennett, personal communication, 1997) for the weak shock event under consideration. The normal determined from the bow shock model along with the upstream magnetic field gives $\theta_{Bn1\,model} \approx 77°$ (indicated by the lower horizontal solid line in Figure 6). It must be noted, however, that the model determination is correct only in an average sense. Both of these independent estimates suggest a shock geometry with a high θ_{Bn1} value. Thus, using these results as a guide, we assume the most probable values for θ_{Bn1} and M_f
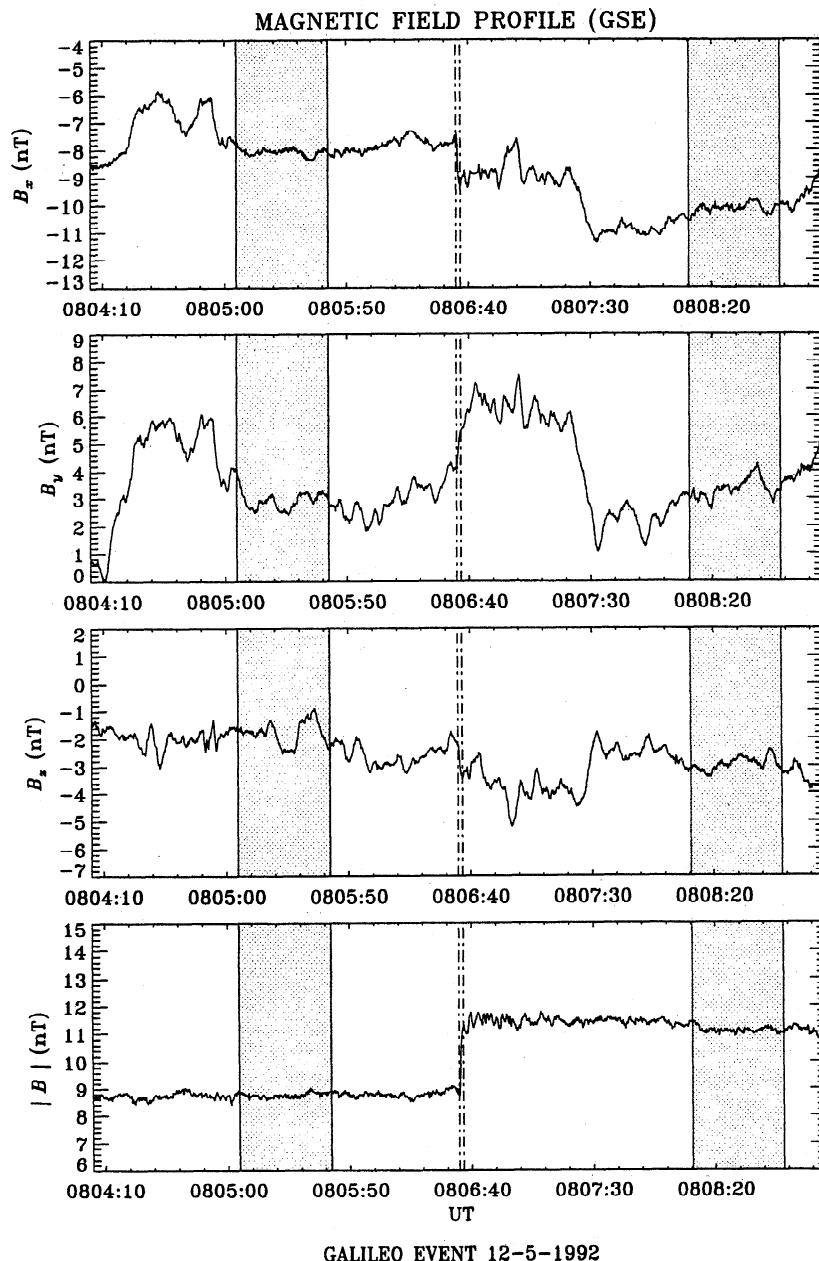
Figure 7. Magnetic field profile of the shock event under investigation. The time intervals of the data samples used in the Vlasov-Liouville mapping are shaded in the figure.

(estimated to be 71° and 1.2, respectively) to test the Vlasov mapping procedure. By using the most probable values for θ_{Bn1} and M_f the Vlasov mapping procedure can be tested by employing a one parameter χ^2 fit for the HTF potential jump [Φ^{HT}] as discussed below. With this choice of parameters, M_A is 1.46, and U_{n1} is 108 km s^{-1}.

The upstream and downstream plasma data sets were chosen to be far enough in the asymptotic regions of the shock so that the instrument collection cycle gives data uncorrupted by the shock layer. The full three-dimensional (3-D) electron distribution functions used in the mappings and comparisons are constructed from particle data sampled over two spin periods ($\simeq$38 s) for

the energy range of 8.5 V to 50 kV (see *Frank et al.* [1992] for details). For the purposes of this study, individual 2.4 s time resolution energy pitch angle samples of the upstream distribution function data are matched with the corresponding magnetometer data to determine the corresponding $v_\parallel, v_\perp$ of the sample. Figure 7 displays the magnetic field profile of the shock event with the selected plasma data intervals used in the mappings.

As mentioned above, the Vlasov mapping is performed in the HTF defined by the geometry and parameters given above. Transformation to the HTF is easily achieved by converting the velocity coordinate of each distribution function data point to the plasma
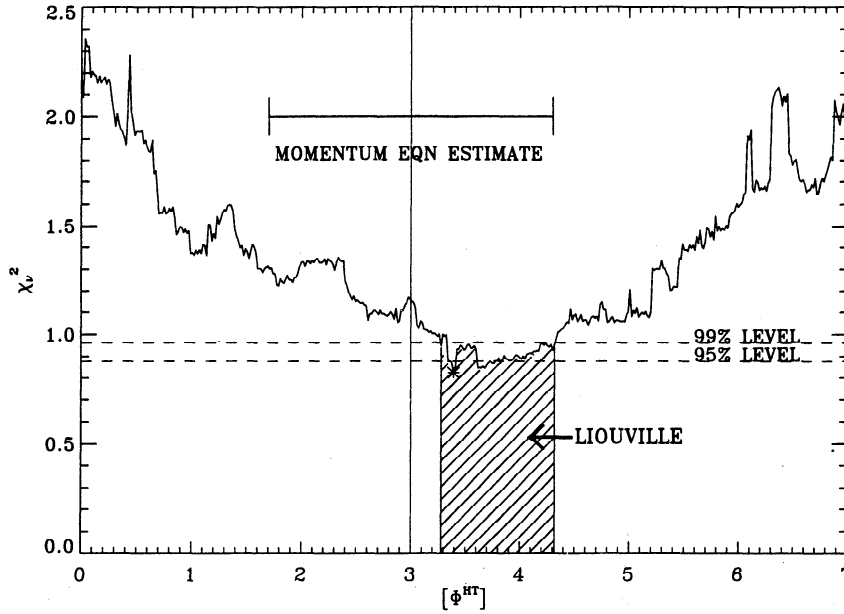
Figure 8. Reduced χ^2 as a function $[\Phi^{HT}]$ shows the range of $[\Phi^{HT}]_{fit}$ (hatched region) selected by Liouville mapping procedure. Also illustrated is a consistent estimate of $[\Phi^{HT}]_{est}$ out to 1 standard deviation (solid vertical line with error bars) independently determined from the electron momentum equation under some simplifying assumptions.

rest frame and then shifting the parallel component of the peculiar speed by the HTF speed $V_1^{HT} = \frac{U_{n1}}{\cos(\theta_{Bn1})}$. Conservation of energy and magnetic moment are used to map the distribution function coordinates to the downstream side of the shock. Bucket averaging is employed to smooth the mapped distribution function and downstream experimental distribution function over the detector energy resolution $\frac{\Delta E}{E} \simeq 0.11$ and angular resolution $\sqrt{\Delta\Omega} \simeq 20°$. In the Vlasov-Liouville mapping of this section the HTF potential jump $[\Phi^{HT}]$ is treated as a free parameter. Changes in $[\Phi^{HT}]$ will affect electron accessibility from the solar wind to the magnetosheath. A one parameter χ^2 fit of the form

$$\chi^2 = \sum_{i=1}^{N} \frac{\left(f_{2_{th_i}}/f_{2_{exp_i}} - 1\right)^2}{\sigma_r^2} \qquad (9)$$

is used to determine $[\Phi^{HT}]$ such that $f_{2_{th_i}}([\Phi^{HT}]) = f_{2_{exp_i}}$. Here $f_{2_{th_i}}$ represents the ith estimate of the theoretically mapped downstream bucket averaged distribution function, and $f_{2_{exp_i}}$ is the corresponding observed downstream bucket averaged distribution function. The σ_r is the error associated with the ratio $f_{2_{th_i}}/f_{2_{exp_i}}$.

5. Results of Mapping Technique Applied to Experimental Distribution Functions

The results of the χ^2 fit procedure are summarized in Figure 8. The asterisk at the minimum of χ^2 corresponds to $[\Phi^{HT}]_{best} \simeq 3.4$ V. Confidence intervals representing possible parameter values out to the 3 standard

deviation limit or 99.6% probability are indicated by the dashed vertical lines in Figure 8. Thus, with 99.6% confidence, $[\Phi^{HT}]_{fit}$ is estimated to be 3.4 $\pm^{0.9}_{0.1}$ V (hatched region) by the Liouville fit procedure. The solid vertical line with error bars in Figure 8 indicates a consistent estimate of $[\Phi^{HT}]_{est}$ independently determined from the ambipolar electric field term of the electron momentum equation under some simplifying assumptions discussed below. While the most probable values for θ_{Bn1} and M_f were used to reduce the mapping problem to a one parameter χ^2 fit procedure, variations in these parameters within the empirical bounds (indicated by level curves of $\mathcal{P}$ in Figure 6) did not significantly change the result of the fit.

Figures 9a and 9b depict comparisons of upstream experimental, downstream experimental, and downstream theoretical $v_\perp = 0$ and $v_\parallel = 0$ cuts of the distribution function in the plasma rest frame, respectively. The dash-dotted curve represents the observed upstream distribution; the dotted curve represents the observed downstream distribution; and the solid curve represents the theoretical downstream distribution determined by employing Liouville's theorem to map the observed upstream electron distribution to the downstream side of the shock. Error bars consistent with the PLS instrument are indicated on the interpolated perpendicular and parallel cuts of the observed downstream distribution function. The theoretically mapped distribution function overlaps the observed downstream distribution function. Of particular interest is the ability of the mapped distribution function to display the preferential perpendicular inflation ($v_\parallel = 0$ cut) with almost no inflation along the magnetic field ($v_\parallel = 0$ cut) as found by observation. Especially noteworthy is that this has
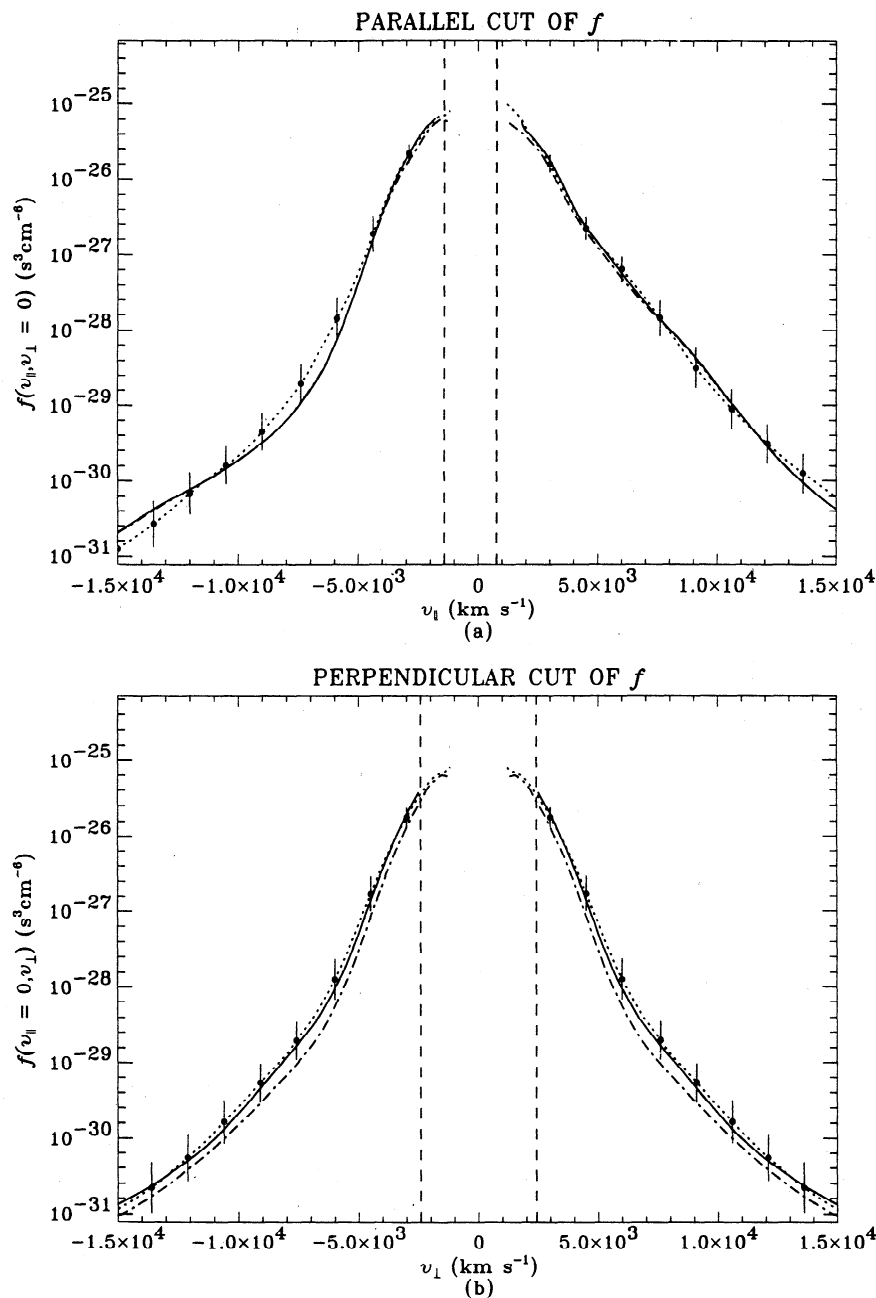
Figure 9. (a) Parallel and (b) perpendicular cuts of the upstream and downstream experimental electron distribution function in the plasma rest frame as compared to the respective cuts of the theoretically mapped downstream electron distribution function. The dash-dotted curve represents the observed upstream distribution function; the dotted curve represents the observed downstream distribution function; and the solid curve represents the theoretical downstream distribution function. The theoretical void is bounded by dashed vertical lines in Figures 9a and 9b. Error bars consistent with the PLS instrument are indicated on the interpolated perpendicular and parallel cuts of the observed downstream distribution function.

been achieved without considering the impact of wave particle interactions. The low-energy cutoff in the measured distributions reflects the PLS energy range of coverage. The low-energy cutoff in the downstream theoretical distribution function reflects the lowest energy sampling of the the upstream distribution function that is accessible to the downstream side. The theoretical void expected from orbits that cannot access the down-

stream side from the upstream boundary is indicated by the dashed vertical lines in Figures 9a and 9b.

Figure 10 compares the downstream theoretically mapped distribution function as determined from the optimal χ^2 fit parameters with the corresponding downstream experimental distribution function. To minimize dispersion caused by interpolation, only energy pitch angle samples that have a correspondence between

$f_{2\ \text{exp}}$ BUCKETS VS $f_{2\ \text{theory}}$ BUCKETS
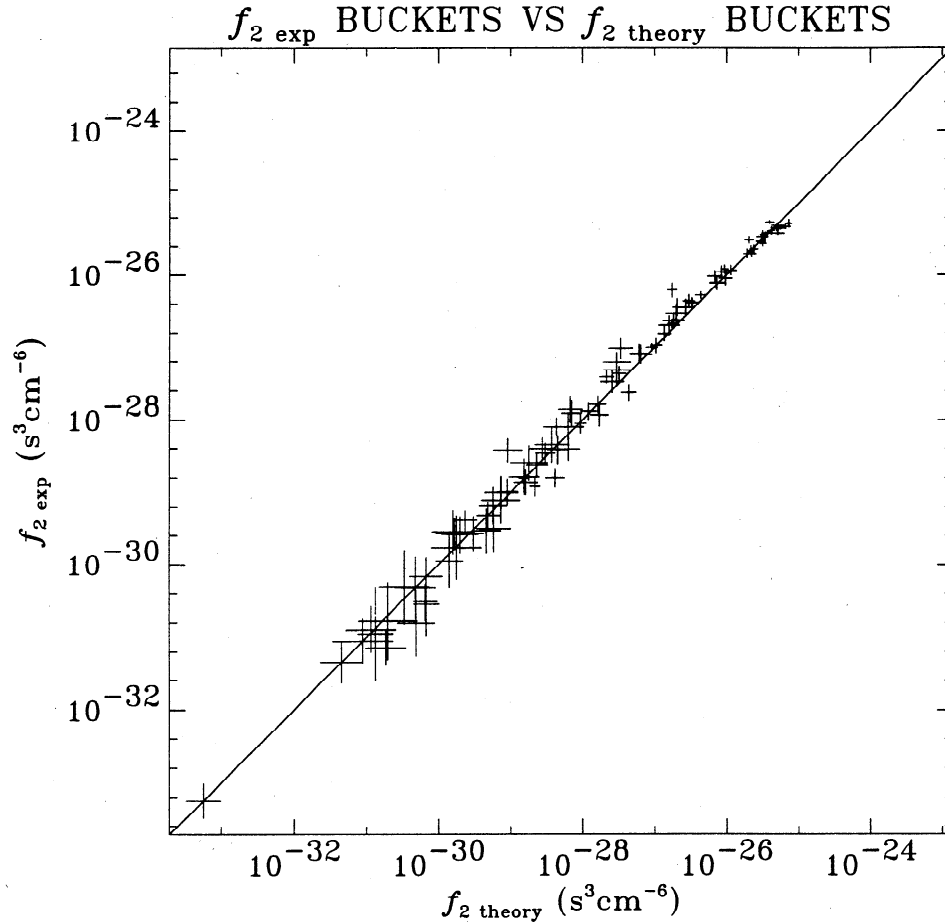
Figure 10. Scatterplot of overlapping bucket averaged theoretical and experimental downstream electron distribution function data points.

the mapped distribution and the observed distribution without interpolation are shown in Figure 10. All pitch angles are almost uniformly represented in Figure 10. Figure 10 illustrates that the theoretically mapped distribution function fits the observed distribution function well at all energies and pitch angles.

To further substantiate the selected value of $[\Phi^{HT}]_{\text{fit}}$, the HTF potential jump was independently estimated from the ambipolar electric field term in the electron momentum equation [*Goodrich and Scudder*, 1984]:

$$\frac{d(e\Phi^{HT})}{ds} \approx \frac{1}{n_e}\left[\frac{dP_{e\|}}{ds} - \left(P_{e\|} - P_{e\perp}\right)\frac{d\ln B}{ds}\right] \quad (10)$$

where n_e is the electron density, $P_{e\perp} = n_e k T_{e\perp}$, $P_{e\|} = n_e k T_{e\|}$ and s is the arc length along the magnetic field. In the weak shock limit, $T_{e\|}$ is approximately constant. If changes of $T_{e\perp}$ were modeled as $T_{e\perp} \propto B$, an estimate of $[\Phi^{HT}]$ from (10) can be obtained. Assuming these relationships are valid within the layer, (10) can be integrated to obtain

$$[\Phi^{HT}]_{\text{est}} \approx \frac{k}{e}\left[T_{e\|_1}\ \ln\left(\frac{n_{e_2}}{n_{e_1}}\frac{B_1}{B_2}\right) + T_{e\perp_1}\left(\frac{B_2}{B_1} - 1\right)\right] \quad (11)$$

The estimate of the HTF potential jump from (11) is 3.0 ± 1.3 V using the experimental data as indicated in

Figure 8. However, (11) is only an estimate of the leading order contribution to the HTF potential jump across the shock layer and is valid only if the assumptions used are valid inside the shock layer. The best determination of $[\Phi^{HT}]$ can come only from model independent integration of the full electron momentum equation through the shock layer using high time resolution plasma data which has only been done once [*Scudder*, 1986a]. Nevertheless, $[\Phi^{HT}]_{\text{est}}$ determined by (11) is consistent with $3.4 \pm ^{0.9}_{0.1}$ V determined by the χ^2 fit procedure, although we believe the χ^2 minimization result to be more accurate given its level of over determinacy from the large number of pitch angle and energy tests performed along separate characteristic bundles. In this sense the phase space map is a bundle of particles probing the potential jump in an over determined way as constrained by the RH jump relations, the magnetic field and density observations.

6. Conclusion

This paper provides further support for the notion that the fully reversible DC electric and magnetic fields acting on magnetized electrons are primarily responsible for the electron velocity distribution signatures and electron heating at strong and weak quasi-perpendicular

fast mode shocks. In particular, the Vlasov-Liouville mapping model which emphasizes the behavior of magnetized electrons in the DC fields can recover the preferential perpendicular inflation signatures observed at weak shocks, as well as the nearly isotropic inflation signatures observed at strong shocks without invoking wave particle effects. Different mechanisms are not required to explain electron heating in these shock limits as suggested by *Feldman et al.* [1983a, b]. The preferential perpendicular heating in the weak shock case and the nearly isotropic heating in the strong shock case can be inferred from the shape of the elliptical void in velocity space determined by (7) with an equality. The void reflects the dispersion or redistribution of the electron phase space as dictated by the DC electric and magnetic fields. Trends in the heating of the electrons in the perpendicular and parallel degrees of freedom at strong and weak collisionless fast mode shocks using a maximal trapping assumption are recovered without invoking wave particle interactions. It is important to note that all shocks require irreversible dissipation. We believe that higher-order irreversible heating/cooling is provided by wave particle interactions which act to smooth the DC inflated distribution function and fill voids of inaccessibility. It should be recalled that the best current evidence shows that wave particle effects cool the electrons rather than heat them [*Scudder et al.*, 1986c].

The Liouville mapping technique has been successfully applied to the full 3-D upstream electron velocity distribution function at a weak collisionless fast mode shock. In particular, the mapping procedure applied to the observed upstream electron distribution reproduces the preferential perpendicular inflation with relatively little inflation parallel to the magnetic field as observed in the downstream electron distribution function (see Figure 9). Moreover, $[\Phi^{HT}]_{fit}$ is consistent with an independent estimate from the ambipolar electric field. The results as applied to a very weak bow shock event also provide a natural explanation for the preferential perpendicular electron heating previously observed at weak interplanetary shocks.

References

Abraham-Shrauner, B., Determination of magnetohydrodynamic shock normals, *J. Geophys. Res.*, *77*, 736-739, 1972.

Alfvén, H., and C. G. Fälthammer, *Cosmical Electrodynamics*, 2nd ed., Clarendon, Oxford, England, 1963.

Balikhin, M., and M. Gedalin, Kinematic mechanism of electron heating in shocks: Theory versus observations, *Geophys. Res. Lett.*, *21*, 841-844, 1994.

Balikhin, M., M. Gedalin, and A. Petrukovich, New mechanism for electron heating in shocks, *Phys. Rev. Lett.*, *70*, 1259-1262, 1993.

Biskamp, D., Collisionless shock waves in plasmas, *Nucl. Fusion*, *13*, 719-740, 1973.

Burlaga, L. F., and K. W. Ogilvie, Solar wind temperature and speed, *J. Geophys. Res.*, *78*, 2028-2034, 1973.

Davidson, R. C., and N. A. Krall, Anomalous transport in high temperature plasmas with applications to solenoidal fusion systems, *Nucl. Fusion*, *17*, 1313-1372, 1977.

Feldman, W. C., J. R. Asbridge, S. J. Bame, M. D. Montgomery, and S. P. Gary, Solar wind electrons, *J. Geophys. Res.*, *80*, 4181-4196, 1975.

Feldman, W. C., R. C. Anderson, S. J. Bame, J. T. Gosling, R. D. Zwickl, and E. J. Smith, Electron velocity distributions near interplanetary shocks, *J. Geophys. Res.*, *88*, 9949-9958, 1983a.

Feldman, W. C., S. J. Bame, S. P. Gary, J. T. Gosling, D. J. McComas, M. F. Thomsen, G. Paschmann, and M. M. Hoppe, Electron velocity distributions near the Earth's bow shock, *J. Geophys. Res.*, *88*, 96-110, 1983b.

Fitzenreiter, R. J., J. D. Scudder, and A. J. Klimas, Three-dimensional analytical model for the spatial variation of the foreshock electron distribution function: Systematics and comparisons with ISEE observations, *J. Geophys. Res.*, *95*, 4155-4173, 1990.

Forslund, D. W., and C. R. Shonk, Formation and structure of electrostatic collisionless shocks, *Phys. Rev. Lett.*, *25*, 1699-1702, 1970.

Frank, L. A., K. L. Ackerson, J. A. Lee, M. R. English, and G. L. Pickett, The plasma instrumentation for the Galileo mission, *Space Sci. Rev.*, *60*, 283-304, 1992.

Galeev, A. A., Collisionless shocks, in *Physics of Solar Planetary Environment*, edited by D. J. Williams, pp. 464-493, AGU, Washington, D. C., 1976.

Goodrich, C. C., Numerical simulations of quasi-perpendicular collisionless shocks, in *Collisionless Shocks in the Heliosphere: Reviews of Current Research, Geophys. Monogr. Ser.*, vol. 35, edited by B. T. Tsurutani and R. G. Stone, pp. 153-168, AGU, Washington, D. C., 1985.

Goodrich, C. C., and J. D. Scudder, The adiabatic energy change of plasma electrons and the frame dependence of the cross shock potential at collisionless magnetosonic shock waves, *J. Geophys. Res.*, *89*, 6654-6662, 1984.

Greenstadt, E. W., and R. W. Fredricks, Shock systems in collisionless space plasmas, in *Solar System Plasma Physics*, edited by I. J. Lanzerotti, C. F. Kennel, and E. N. Parker, vol. III, pp. 5-43, North-Holland, New York, 1979.

Kivelson, M. G., K. K. Khurana, J. D. Means, C. T. Russell, and R. C. Snare, The Galileo magnetic field investigation, *Space Sci. Rev.*, *60*, 357-383, 1992.

Kivelson, M. G., A. Prevost, F. V. Coroniti, K. K. Khurana, and D. J. Southwood, Galileo flybys of Earth: The nature of the distant shock, *Adv. Space Res.*, *16*(4), 197-204, 1995.

Knight, S., Parallel electric fields, *Planet. Space Sci.*, *21*, 741-750, 1973.

Krauss-Varban, D., F. G. E. Pantellini, and D. Burgess, Electron dynamics and whistler waves at quasi-perpendicular shocks, *Geophys. Res. Lett.*, *22*, 2091-2094, 1995.

Lepping, R. P., and P. D. Argentiero, Single spacecraft method of estimating shock normals, *J. Geophys. Res.*, *76*, 4349-4359, 1971.

Leroy, M. M., and D. Winske, Backstreaming ions from oblique Earth bow shocks, *Ann. Geophys*, *1*, 527-536, 1983.

Leroy, M. M., D. Winske, C. C. Goodrich, C. S. Wu, and

K. Papadopoulos, The structure of perpendicular bow shocks, *J. Geophys. Res.*, *87*, 5081-5094, 1982.

Montgomery, M. D., J. R. Asbridge, and S. J. Bame, Vela 4 plasma observations near the Earth's bow shock, *J. Geophys. Res.*, *75*, 1217-1230, 1970.

Morse, R. L., Adiabatic time development of plasma sheaths, *Phys. Fluids*, *8*, 308-314, 1965.

Papadopoulos, K., A review of anomalous resistivity for the ionosphere, *Rev. Geophys.*, *15*, 113-127, 1977.

Russell, C. T., M. M. Hoppe, W. A. Livesey, J. T. Gosling, and S. J. Bame, ISEE 1-2 Observations of laminar bow shocks: Velocity and thickness, *Geophys. Res. Lett.*, *9*, 1171-1174, 1982.

Savoini, P., and B. Lembege., Electron dynamics in two and one dimensional oblique supercritical collisionless magnetosonic shocks, *J. Geophys. Res.*, , *99*, 6609-6635, 1994.

Schwartz, S. J., M. F. Thomsen, S. J. Bame, and J. T. Stansberry, Electron heating and the potential jump across fast mode shocks, *J. Geophys. Res.*, *93*, 12,923-12,931, 1988.

Schwartz, S. J., M. F. Thomsen, W. C. Feldman, and F. T. Douglas, Electron heating and potential jump across slow mode shocks, *J. Geophys. Res.*, *92*, 3165-3174, 1987.

Scudder, J. D., A review of the physics of electron heating at collisionless shocks, *Adv. Space Res.*, *15*(8/9), 181-223, 1995.

Scudder, J. D., The field-aligned flow approximation for electrons within layers possessing a normal mass flux: A corollary to the deHoffmann-Teller theorem, *J. Geophys. Res.*, *92*, 13,447-13,455, 1987.

Scudder, J. D., A. Mangeney, C. Lacombe, C. C. Harvey, T. L. Aggson, R.R. Anderson, J. T. Gosling, G. Paschmann, and C. T. Russell, The resolved layer of a collisionless, high β, supercritical, quasi-perpendicular shock wave, 1, Rankine-Hugoniot geometry, currents and stationarity, *J. Geophys. Res.*, *91*, 11,019-11,052, 1986a.

Scudder, J. D., A. Mangeney, C. Lacombe, C. C. Harvey, and T. L. Aggson, The resolved layer of a collisionless,

high β, supercritical, quasi-perpendicular shock wave, 2, Dissipative fluid electrodynamics, *J. Geophys. Res.*, *91*, 11,053-11,073, 1986b.

Scudder, J. D., A. Mangeney, C. Lacombe, C. C. Harvey, C.S. Wu, and R.R. Anderson, The resolved layer of a collisionless, high β, supercritical, quasi-perpendicular shock wave, 3, Vlasov electrodynamics, *J. Geophys. Res.*, *91*, 11,074-11,097, 1986c.

Whang, Y. C., Slow shocks and their transition to fast shocks in the inner solar wind, *J. Geophys. Res.*, *92*, 4349-4356, 1987.

Whipple, E. C., The signature of parallel electric fields, *J. Geophys. Res.*, *82*, 1525-1531, 1977.

Winske, D., J. Giacalone, M. F. Thomsen, and M. M. Mellott, A comparative study of plasma heating by ion acoustic and modified two-stream instabilities at subcritical quasi-perpendicular shocks, *J. Geophys. Res.*, *92*, 4411-4422, 1987.

Winske, D., M. Tanaka, C. S. Wu, and K. B. Quest, Plasma heating at collisionless shocks due to the kinetic cross-field streaming instability, *J. Geophys. Res.*, *90*, 123-136, 1985.

Wu, C. S., D. Winske, Y. M. Zhou, S. T. Tsai, P. Rodriguez, M. Tanaka, K Papadopoulos, K. Akimoto, C. S. Lin, M. M. Leroy, and C. C. Goodrich, Microinstabilities associated with a high Mach-number, perpendicular shock, *Space Sci. Rev.*, *37*, 63-109, 1984.

L.A. Frank, A.J. Hull, W.R. Paterson, and J.D. Scudder, Department of Physics and Astronomy, University of Iowa, Iowa City, IA 52242. (e-mail: frankAiowasp.physics.uiowa.edu: ajh@hydra.physics.uiowa.edu; paterson@iowasp.physics.uiowa.edu: jds@hydra.physics.uiowa.edu)

M.G. Kivelson, Institute of Geophysics and Planetary Physics, University of California, Los Angeles, CA 90095. (e-mail: mkivelson@igpp.ucla.edu)